An electrooptically modulated birefringent filter for absolute infrared thermography

J. Howard

Plasma Research Laboratory,

Australian National University. Canberra ACT 0200

Abstract

We describe a wide field-of-view large aperture electro-optically modulated infrared filter spectrometer (MIRF) for estimation of absolute blackbody temperatures. Based on birefringent lithium tantalate crystals, the visibility of interference fringes generated by the electrooptic modulation can be related directly to the blackbody radiation temperature, without regard to the spatial variation of the surface emissivity or need for absolute sensitivity calibration. When combined with a mid-IR imaging camera and appropriate software, the system can, in principle, deliver time resolved temperature contours of the radiating body. As with other techniques that rely on spectral shape estimation of the temperature, the MIRF spectrometer is not as sensitive to temperature changes as a brightness radiometer. However, for high resolution applications, the filter can be used for in-line routine absolute calibration of sensitive IR cameras that sense only "brightness temperature" variations. We describe single channel and imaging instruments that can be configured for estimating blackbody temperatures from emission peaking in the infrared through to visible.

Contents

1   Introduction

Non-contact optical thermometry is a rapidly growing field with applications in remote-sensing of hostile or corrosive environments, medical imaging, environmental studies and industrial process monitoring. Although the current state-of-the-art relies on cryogenic radiometers, uncertainties related to details of surface emissivity still pose a problem for absolute temperature estimation. Spectral techniques based on Michelson interferometers and two-colour pyrometry are still preferred in many applications. Though not as sensitive to small temperature changes as radiometers, spectral techniques are now achieving sub-degree temperature resolution [1].

The modulated infrared filter spectrometer (MIRF spectrometer) is a new instrument concept for absolute remote theromography. Since it is a spectrally discriminating device it does not require absolute intensity calibration as is the case for radiometric based instruments such as IR cameras. On the other hand it is much simpler and more compact than Fourier transform infrared (FTIR) spectrometers to which it is related. It is easily adapted to imaging infrared cameras and suffers none of the drifts, discretization errors or long-term stability problems associated with Michelson FTIR interferometers. MIRF is based on electrooptically modulatable lithium tantalate crystals set between polarizing plates. It monitors the first spectral moment of the emission spectrum within a specified passband determined by the expected source temperature.

The blackbody spectral radiance is a universal single parameter distribution governed by the temperature T of the radiating source (see Fig. 1):

$$L_\lambda(\lambda; T) = \frac{2hc^2}{\lambda^5} \frac{1}{\exp\left(hc/\lambda kT\right) - 1}. \tag{1}$$

Integrated over wavelength, the total power radiated by a surface of area A and emissivitiy ϵ at temperature T is given by

$$P = \epsilon A \sigma T^4 \tag{2}$$

where σ is the Stephan-Boltzmann constant. In general, the emissivity $\epsilon(\lambda, T)$ can be dependent on both wavelength and temperature.

Within a narrow fixed wavelength band, the emission intensity is a strong function of temperature. Based on this fact, narrowband radiometric methods for temperature estimation require knowledge of the absolute sensitivity of the detection system as well as an estimate of the surface emissivity.

An alternative method to estimate temperature absolutely is to fit the spectral shape of the blackbody curve, or to accurately estimate the wavelength of peak emission λ_M given by Wein's displacement law

$$\lambda_M T = 2.898 \times 10^{-3} \text{ m K}. \tag{3}$$

Determining λ_M or some spectral quantity related to it, allows to infer the temperature of the source. This approach relies on being able to treat the radiation source as a greybody in the sense that the spectral variation of the emissivity is unimportant in the region of interest. Spectral estimation of source temperatures can be obtained using Fourier-transform infrared (FTIR) spectroscopy or two-color radiometry. These approaches are described in more detail in Sec. 2.

Our approach is a hybrid of FTIR and two-color techniques based on electrooptic and birefringent infrared-visible crystals. It is an extension of the high resolution MOSS spectrometer to broadband infrared applications. The so-called MOSS (modulated optical solid-state) spectrometer monitors the complex coherence (fringe visibility and phase) of an isolated spectral line at one or more optical delays and has been used recently for visible light Doppler imaging of high temperature plasmas in the H-1 heliac [2, 3].
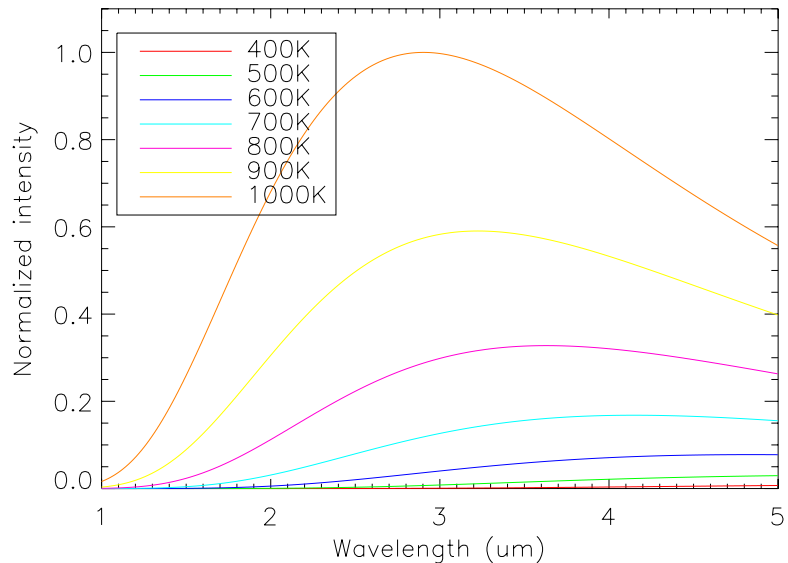
A patent application (No. 83248/98) has been filed for MOSS. To date a single channel unit has been sold to Princeton Plasma Physics Laboratory. Negotiations are underway with the Institute for Plasma Physics in Germany for the construction and sale of a multi-channel MOSS camera for installation on one of their plasma devices. This is an extremely positive development that arose, in part, from an invited presentation made to the APS Topical Conference on High Temperature Plasma Diagnostics at Tuscon in June 2000. More information about MOSS systems can be found at `http://rsphysse.anu.edu.au/prl/MOSS.html`.

MOSS is suited to high-resolution studies of spectral lineshape. In this work we consider the utility of electrooptic birefringent plate interferometers for relatively low resolution spectral applications such as the measurement of broadband infrared blackbody radiation. The measurement principles (outlined in Sec. 3), implementation and associated instrumental issues are significantly different from the MOSS system.
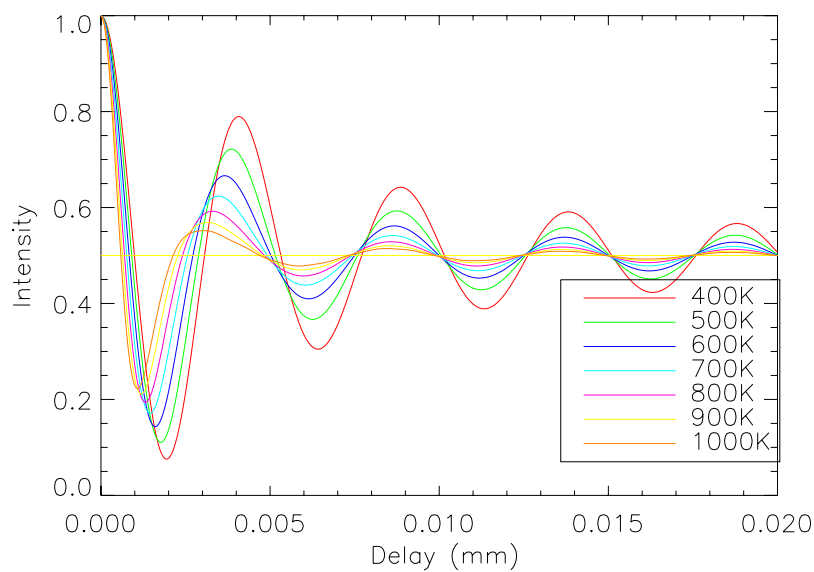
The proposed Modulated Infrared Filter Spectrometer is compact and robust and, because it uses transmission based optics, can be readily mounted to the front of an IR imaging camera. In this sense, it promises a relatively inexpensive and portable alternative to mechanically scanned FTIR systems, capable of producing absolute temperature images for condition monitoring of furnaces and kilns as well as remote inspection, for example, of plasma facing components and antenna systems in fusion devices. For high resolution thermography, MIRF can be used as a convenient tool for absolute calibration of the IR camera. In Sec. 4. we focus on the mid-IR range from 1-5 μm for accurate temperature sensing in the range 300-1000K. The ideas can be readily extended to the near-IR and visible for higher temperature applications (Sec. 5). Some preliminary experimental results confirming the instrument performance at higher temperatures are presented in Sec. 6. Imaging MIRF systems are are described in Sec. 7 while thermal imaging applications for MIRF-based systems are summarized in Sec. 8.

Finally, it is worth noting that the Defence Science and Technology Organisation in Salisbury are currently seeking internal funding support (initially $80 K)

4

for a variant of MIRF that will enbale discrimination of missile/aircraft engine infrared spectral signatures. Though the measurement principle is different to that described here for estimating blackbody temperatures, the hardware and optics are almost identical.

(a)

(b)

Figure 1: (a) Blackbody emission spectrum in the 1-5 μm band for temperatures spanning the range 400-1000K (b) Fourier transform of the emission spectra in (a). A top-hat bandpass filter spanning the range 1-5 μm has been applied. The delay coordinate is expressed in terms of an equivalent free-space interferometer mirror separation

2 State of the art

2.1 Infrared radiometry

Infrared radiometers are passive sensors operating at wavelengths near 10 μm that measure the "brightness temperature" of the naturally occurring infrared radiation in the environment. The brightness temperature is equal to the physical temperature for a perfect blackbody (an object with 100% emissivity), but is less than the physical temperature for an object with lower emissivitiy.

If the source temperature increases incrementally by ΔT, the radiant intensity also increases according to Eq. (1) so that

$$\frac{\Delta L_\lambda}{L_\lambda} = \rho(\lambda;T)\frac{\Delta T}{T} \tag{4}$$

where

$$\begin{aligned} \rho(\lambda;T) &\equiv \frac{T}{L_\lambda}\frac{\partial L_\lambda}{\partial T} \\ &= \frac{x\exp x}{\exp x - 1} \end{aligned} \tag{5}$$

and we have written $x = hc/\lambda kT$. The temperature sensitivity for a radiometer is determined by its ability to resolve small changes in the radiant emission against background noise. Using sensitive cryogenic quantum well infrared photodetectors (QWIP), temperature sensitivity can be better than $0.02\,^\circ$C.

If the emissivity factor is included, the dependence of the temperature uncertainty on errors in the estimated emissivity is given by

$$\frac{\mathrm{d}\epsilon}{\epsilon} = \rho(\lambda;T)\frac{\Delta T}{T}. \tag{6}$$

The functional form of the factor $\rho(\lambda;T)$ (see Fig. 2) shows that a 10% inaccuracy in the estimate of emissivity can give rise to not insubstantial errors of order a few percent in the inferred temperature. For similar reasons, if the radiating source does not fill the field-of-view of the measurement system, the inferred temeprature can be substantially in error. For these reasons, methods which rely on the spectral information are preferred in many applications.

2.2 Spectral techniques - two-colour pyrometry

It is possible to infer temperature by measuring the ratio of the source radiation intensity at two independent wavelengths and using Planck's radiation law [Eq. (1)]. This approach obviates the need for knowledge of the emissivity or its temperature variation, but requires either for the body to be grey $\epsilon(\lambda) = \epsilon$ or for the spectral dependence of ϵ to be known. As well as reduced sensitivity to emissivity, ratio thermometers are insensitive to obscuration of the field-of-view due, for example, to dust, smoke, obstruction or lens contamination.
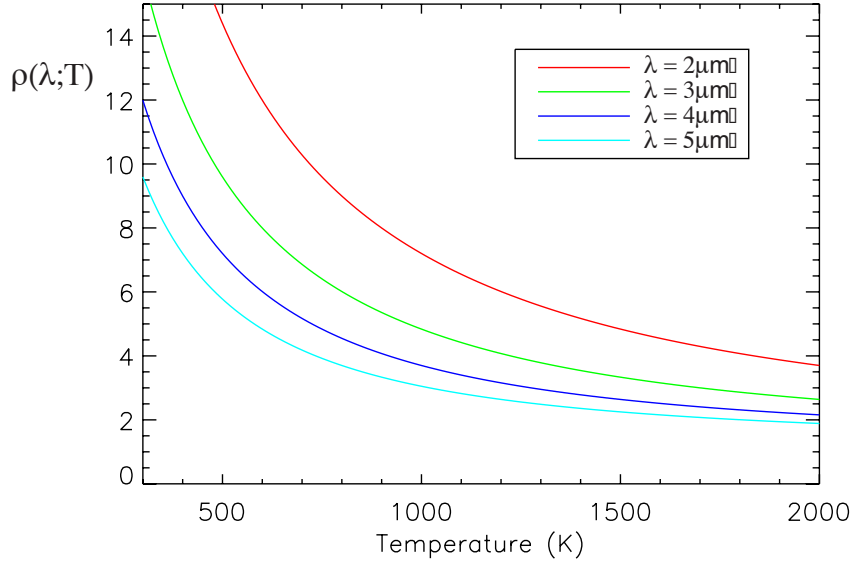
Figure 2: Variation of radiometric temperature sensitivity factor $\rho(\lambda; T)$ as a function of temperature for selected wavelengths 2,3 and 4 μm.

2.3   Spectral techniques - FTIR

Fourier transform spectrometers (FTS) are usually configured as Michelson interferometers in which the translation of one of the mirrors (often piezoelectrically actuated) produces an interference pattern that is registered by a detector or detector array. The ideal FTS signal intensity (interferogram) can be expressed as

$$S_{\pm}(\tau) = \frac{I_0}{2}\left[1 \pm \Re[\gamma(\tau)]\right] \tag{7}$$

where $I_0(\boldsymbol{r})$ is the spectrally integrated emission intensity, τ is the optical path length time delay between the interfering beams and $\gamma(\tau)$ is the optical coherence, related to the light spectral radiance $L_\nu(\nu)$ through the Weiner-Khinchine theorem

$$\gamma(\tau) = \int_{-\infty}^{\infty} L_\nu(\nu) \exp(i2\pi\nu\tau) \, d\nu. \tag{8}$$

($L_\nu(\nu)$ denotes the blackbody spectrum in the optical frequency domain.) In practice, the maximum fringe visibility is reduced by the instrument spectral repsonse to less than unity. This is accounted by multiplying the complex coherence γ by the instrument coherence $\gamma_I = \zeta_I \exp(i\phi_I)$ where $\zeta_I < 1$ is the instrument contrast and ϕ_I the instrument phase.

Figure 1(b) shows the computed Fourier transform of the blackbody spectra of Fig. 1(a) after windowing by a top-hat filter of spectral passband 1-5 μm. As expected, the first zero of the interferogram around 1 μm pathlength delay, shifts

7

to smaller delays as temperature increases (λ_M decreases). Also note that the fringe visibility decreases at higher temperatures (more of the passband is filled).

For optimum performance, FTIRs must be carefully aligned. They can also be bulky and sensitive to external noise, and require a computer for inversion/display of the interferogram. They are not readily configurable as imaging devices, have limited field-of-view, and usually require path length monitoring using a suitable fixed wavelength source such as a laser. An example of a laboratory FTIR for infrared spectroscopy is shown in Fig. 3.

Figure 3: A typical FTIR station

3 MIRF measurement principle

Because of the slowly varying nature of the blackbody spectrum, accurate estimation of λ_M requires measurements over a significant spectral region. On the other hand, by the complementarity of time and frequency domain systems, shifts in λ_M are manifest over a small range of optical delay that can be probed electrooptically. Since the spectral bandwidth required to characterise the blackbody temperature is wide, the temporal coherence is small and most of the spectral information resides in the interferogram close to zero delay. Thus, the first spectral moment of the radiation received in a given spectral passband (related to λ_M), is conveyed by a single measure of the interferogram, namely its slope at

zero delay. The effective spectral width of the received radiation is carried by the curvature (second derivative) of the interferogram at zero delay. Both of these quantities vary with temperature. For small interferometer delays, the blackbody interferogram exhibits a smooth and regular variation with temperature (see Fig. 1(b)). This fact underpins our idea for a modulated birefringent filter that allows to measure a single quantity closely related to the slope/curvature of the interferogram near zero delay. This in turn provides a direct, robust and unambiguous measure for the source temperature.

To illustrate the robustness of this measure, we have corrupted the spectra of Fig. 1 with 20% Poisson noise as shown in Fig. 4 (a) and recomputed the Fourier transform shown in Fig. 4 (b). It is clear that the interferometric information at small delays (dominated by low order spectral moments) is substantially immune to variations in the fine details of the incident light spectrum.

Figure 1(b) shows that the important interferometric information resides within a single interference fringe of zero delay. There are three clear strategies for extracting this information:

(a) Measure the slope of the interferogram within the first half cycle,

(b) probe the position of the first turning point, or

(c) measure the position of the zero crossings

In each case, different optical, modulation and processing schemes are required to extract the information. It remains to be determined which method is best suited to a given application.

The slope of the interferogram can be measured by modulating the interferometer path difference about an appropriate offset (say 0.8 μm in Fig. 1(b)). This will generate a modulation in the light intensity sensed by the detector. As we show below, the temporal properties of this modulation can be used to estimate the source temperature.

Importantly, for all modulation strategies, the temperature information can be encoded at frequencies away from the low-frequency "$1/f$", or flicker noise associated with photoconductors. Moreover, modulation of the signal allows the use of synchronous detection techniques to improve signal to noise ratio (SNR) which is inversely proportional to the square root of the detection bandwidth.

3.1 MIRF construction

In order to overcome problems relating to mechanical and thermal stability as well as vibrations and acoustic noise, a preferred construction for the interferometer uses solid birefringent optical components (to obtain the optical delay) sandwiched between broadband (> 1 μm) wire grid, plate or dielectric polarizers. The optical delay is given by $\tau = LB(\lambda)/c$ where L is the thickness of
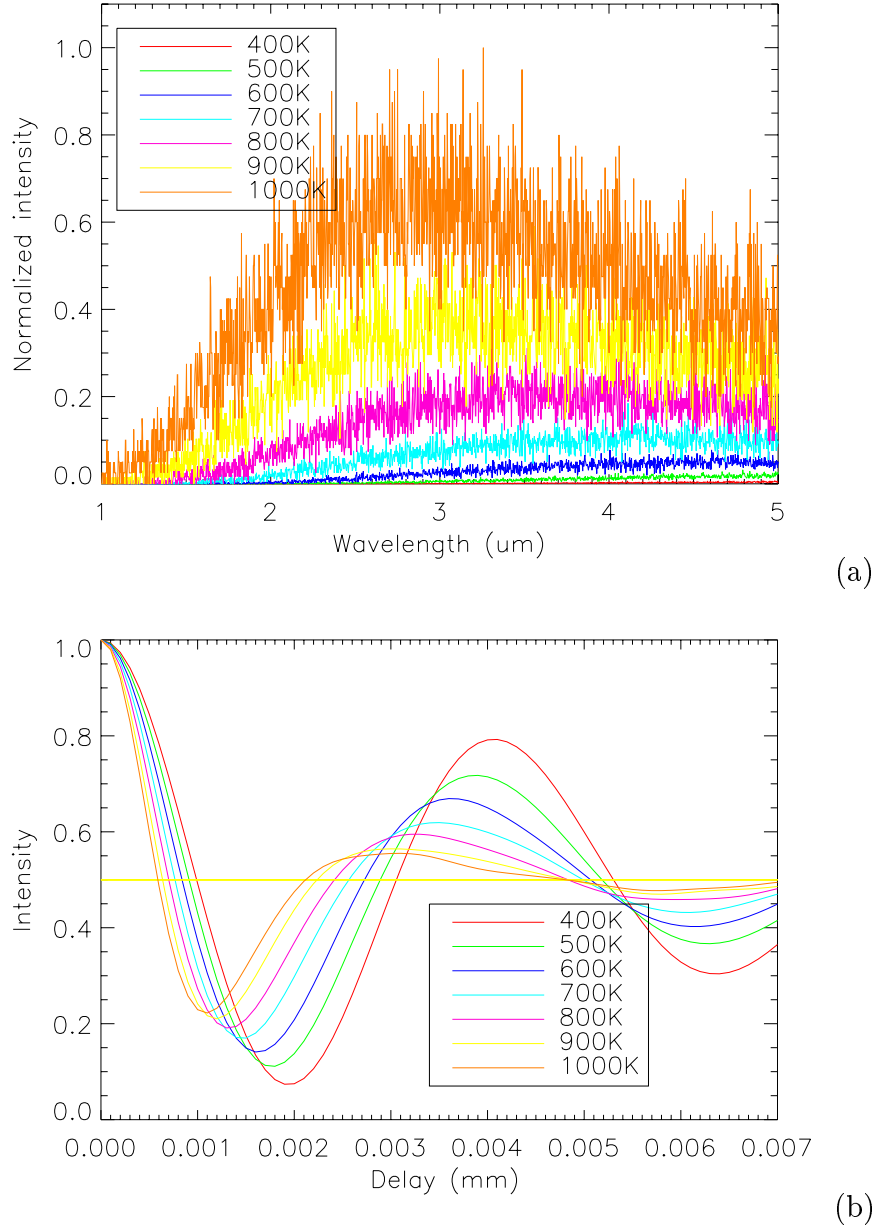
Figure 4: Noise corrupted blackbody spectrum (a) and its Fourier transform (b). The interferogram remains largely uncorrupted at small delay.

the crystal in the direction of propagation and $B(\lambda) = n_E(\lambda) - n_O(\lambda)$ is the crystal birefringence. If the crystals are also electro-optic, the birefringence, and hence the path length delay, can be modulated to generate a time varying signal (interferogram) at the detector. An interference filter (or the natural passband of the optical components/detectors) can be used to select the spectral region of interest. Light can be coupled to the instrument directly or using an optical

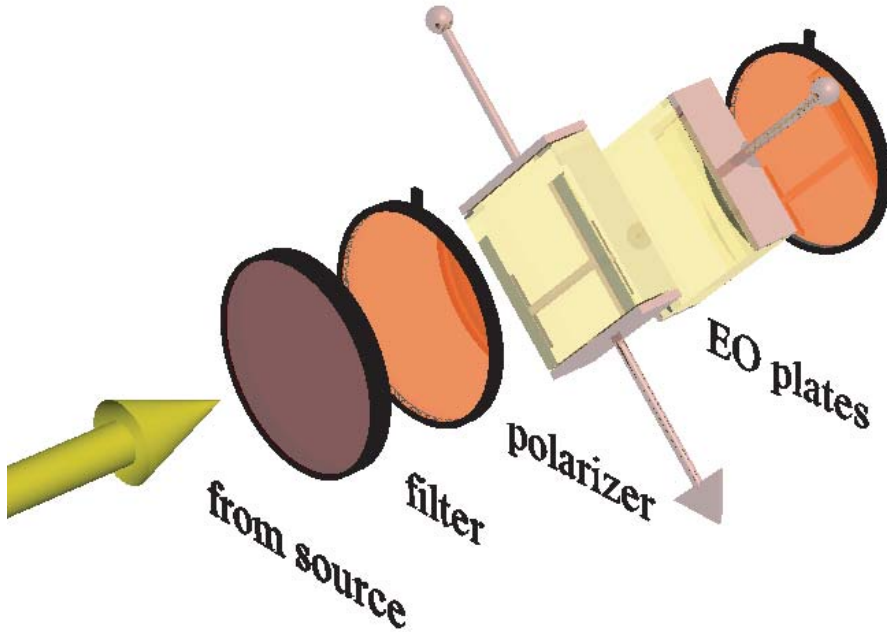fibre/collimating lens combination. A schematic of the electrooptic birefringent filter is given in Fig. 5

Figure 5: Optical layout for the Modulated Infrared Filter Spectrometer.

Both lithium niobate LiNbO$_3$ and lithium tantalate LiTaO$_3$are suitable materials for this purpose, being electrooptic, birefringent and transparent from the visible through to 5 μm. However, because the optical path length delays involved are small, LiTaO$_3$which is weakly birefringent (B=.0045 at 3μm), appears to be the more suitable candidate - tolerances on crystal thicknesses are loose and small crystal delays imply a wide field-of-view (more below). Fig. 6(a) shows the wavelength dependence of the birefringence for LiTaO$_3$[4] and the absorption coefficients for lithium niobate. (Though the transmission properties are similar for lithium tantalate, measured curves have been difficult to obtain).

These uniaxial crystals are naturally birefringent for light propagating along the crystal Y-axis (so called Y-cut). The birefrigence can be modified by applying an electric field in the Z-direction, parallel to the crystal fast axis, and transverse to the direction of propagation. For an applied electric field $E = V/d$, where V is the voltage across the crystal and d is the crystal aperture, the phase delay

11

modulation for propagation along the crystal Y-axis is given by

$$\phi_1 = \frac{\pi E L \delta}{\lambda} \tag{9}$$

where $\delta = (n_E^3 r_{33} - n_O^3 r_{13})$ and r_{33} and r_{13} are electrooptic tensor coefficients. The phase modulation depth can be expessed as an effective crystal thickness modulation

$$\Delta L = \frac{E L \delta}{2B} \tag{10}$$

that is approximately wavelength independent.

Combining two such crystals with their fast axes mutually oriented at 90° but modulated with opposite polarity, will subtract their respective delays (to give a small nett delay L_0) while adding the modulation component (to improve the modulation depth). The sinusoidal modulation drive voltage can be generated using a simple function generator, stereo audio amplifier and step-up transformer. The modulation frequency can be chosen to match the time resolution/hardware requirements dictated by the application.

An alternative to crossed Y-cut birefringent plates is to propagate the light along the electrooptic plate Z-axis (Z-cut). In this case, there is no natural birefringence, so that the required nett optical delay L_0 must be introduced using an additional Y-cut plate. Nevertheless, an electric field applied along the Y-axis of the Z-cut crystal, will induce a birefringence that can be used to modulate the path length delay [5]. Though the drive voltages in this case, can be 30% higher than for crossed Y-cut crystals, the field-of-view is not compromised by the natural birefringence in this orientation. The effect is discussed in more detail in Sec. 7.1.
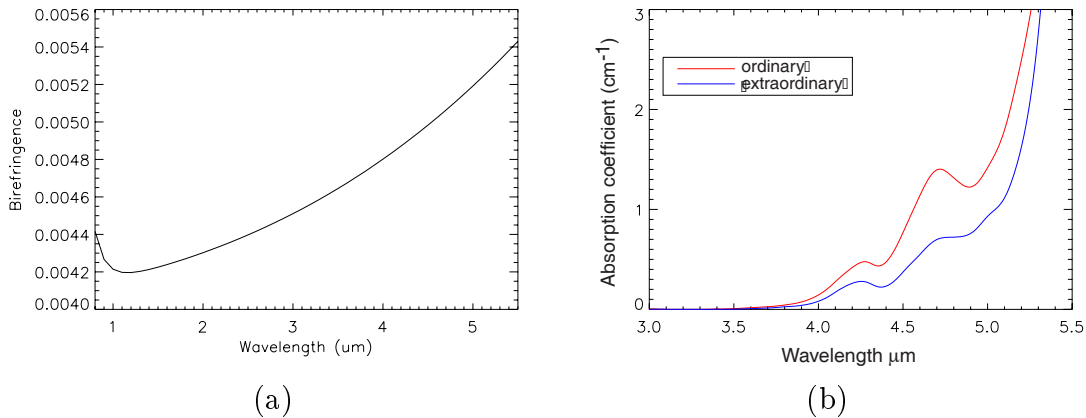

Figure 6: (a) Wavelength dependence of the birefringence for lithium tantalate. (b) Wavelength dependence of lithium niobate coefficient for ordinary and extraordinary rays (courtesy Randy Stanley, `http://www.crystaltechnology.com`). Lithium tantalate should be similar.

4   Measuring temperatures less than 1000K

We have computed the MIRF interferogram for the spectra of Fig. 1(a) including birefringence dispersion and plotted the result as a function of net crystal thickness in Fig. 7. At lower temperatures, the radiance peaks in the mid-IR region of the spectrum (1-5 μm). At these long wavelengths, and for reasonable crystal lengths, only a fraction of the interferogram can be probed electrooptically.

4.1   Measurement strategy (a) - monitoring the slope

As indicated above, it is the shape of the interferogram near zero delay that is most closely related to the source temperature. We therefore choose the offset delay, or operating point, below the first interferogram zero. This appears to be a reasonable compromise between wide temperature dynamic range and acceptable sensitivity. The slope of the interferogram increases with temperature, while the fringe visibility decreases. These two effects work in concert so that the "visibility"

$$\zeta = \frac{S_{\max} - S_{\min}}{S_{\max} + S_{\min}} \tag{11}$$

increases monotonically with temperature. Since the received intensity depends on the emissivity and is strongly temperature dependent, we require a normalized measure to indicate the absolute temperature.

The visibility ζ is roughly proportional to the amplitude of the delay modulation while the operating point can also be optimized for greater sensitivity to temperature changes within a certain temperature interval, but with smaller temperature dynamic range. These aspects are quantified below. We have numerically modelled the signal generated by electrooptical refractive index modulation. For a given applied electric field, we calculate the wavelength dependent phase delay Eq. (9), apply this to the bandpass filtered ideal blackbody spectral radiance L_λ and compute the resulting Fourier transform using Eq. (8).

The EO tensor coefficients for both LiNbO$_3$ and LiTaO$_3$are comparable, with $r_{33} \approx 30$ pm/V and $r_{13} \approx 8$ pm/V. Using $d = 25$ mm aperture optics, an applied voltage of 3000V across two crossed plates each of thickness $L \approx 10$ mm will generate an effective crystal thickness modulation amplitude of 50 μm. (These voltages can be reduced by either reducing the aperture or by increasing the crystal length. The latter can affect the field-of-view as discussed in Sec. 7.1). The resulting time-domain interferograms are shown in Fig. 8(a). The operating point (hereafter taken as the minimum delay excursion during a modulation cycle) corresponds to an effective crystal thickness of $L_0 = 70\mu$m The applied modulation thus covers the delay range from 70 μm to 170 μm.

The "visibility" ζ given by Eq. (11) is calculated from the minimum and maximum signal excursions obtained during a modulation cycle. Figure 8 shows the modulation amplitude dependence of ζ for operating points $L_0 = 70$ μm and
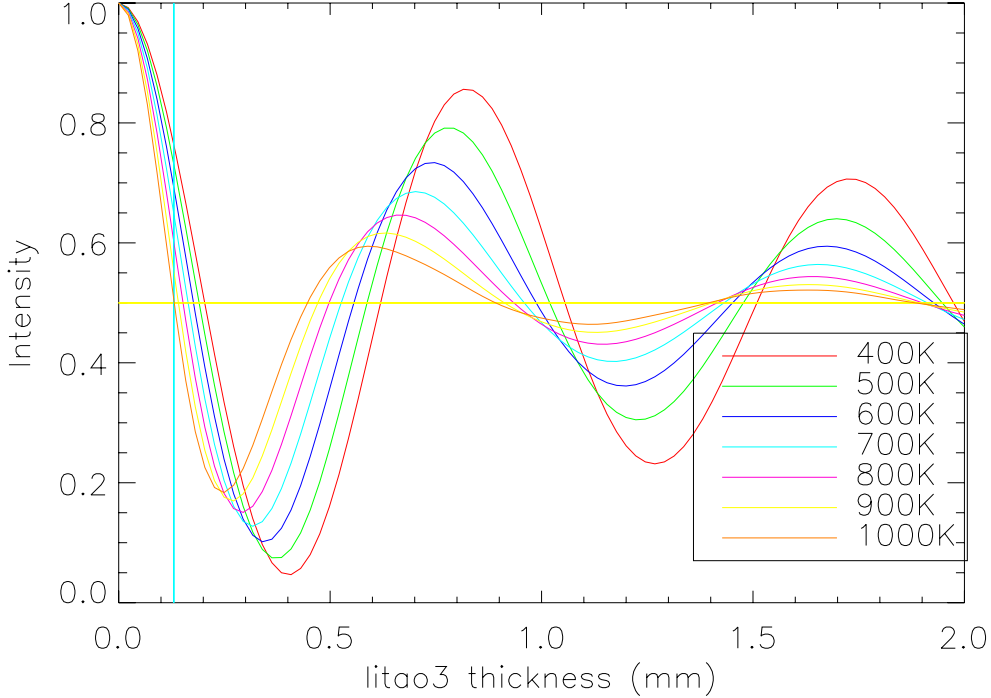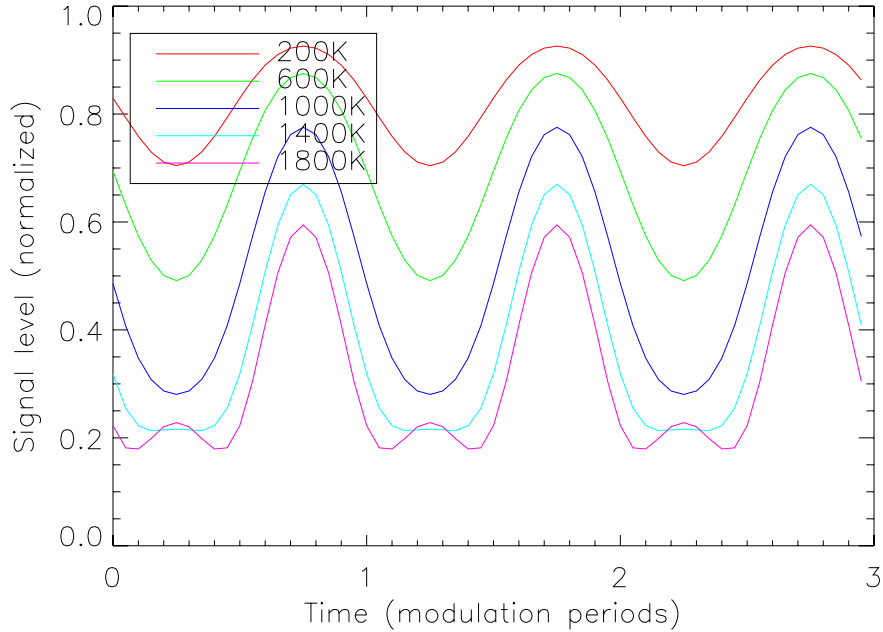
Figure 7: Fourier transform of the emission spectra of Fig. 1. A top-hat bandpass filter spanning the range 1-5 μm has been applied. The delay coordinate is expressed in terms of an equivalent thickness of LiTaO$_3$as discussed in the text.

$L_0 = 40$ μm. The calculations indicate that temperature sensitivity is more dependent on the applied modulation voltage than on the operating point which can also be electrooptically tuned within a reasonable range by applying an appropriate DC bias voltage. Larger tuning steps can be obtained using insertable delay plates either singly or in combination.
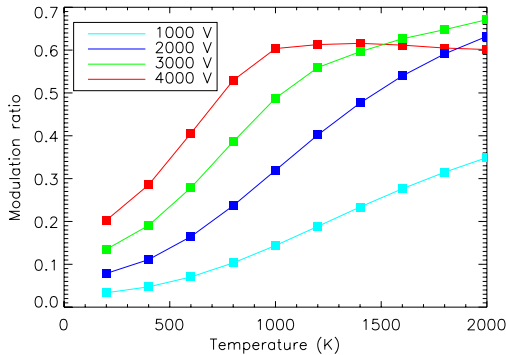
Higher harmonic components of the modulation frequency are generated at higher temperatures. This occurs when the electrooptic delay scan encounters a turning point in the interferogram and becomes more apparent when the modulating voltage is large. This is the essence of measurement strategy (b) mentioned above: the ratio of first and second harmonics of the modulation frequency is a sensitive measure of the position of the turning point and can also be used to estimate temperature as shown in Sec. 5.1.

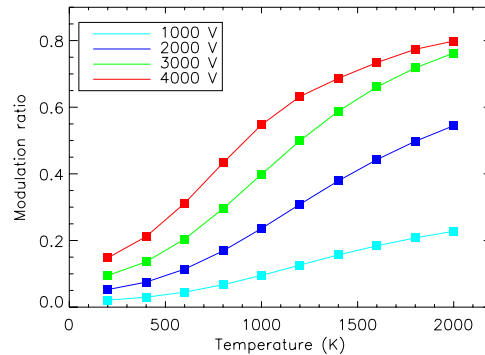## 4.2   Electrooptic tuning of the dynamic range

It will be noticed that the light intensity transmitted by the birefringent filter varies in a quasi-sinusoidal way with delay offset (see Fig. 7). It is therefore possible to control the light throughput of the filter by applying an appropriate

(a)

(a)   (b)

Figure 8: (a) Three modulation periods of the time-domain signal generated by applying a sinusoidal modulating voltage across the lithium tantalate birefringent plates for a range of blackbody temperatures. The signal becomes distorted as the delay modulation scans over the interferogram minimum at higher source temperatures. (b) The visibility versus source temperature for a range of applied voltages and for an operating point (minimum delay) of $L_0 = 70\mu$m. (c) As for (b) but with $L_0 = 40\mu$m. The temperature sensitivity is not a strong function of delay offset.

dc tuning voltage across the crystal plate. Tuning to an interference minimum could help prevent detector saturation and thereby increase the effective detection dynamic range when attempting to measure a source whose temperature (and hence radiant intensity $\propto T^4$) might vary significantly. Such a dc voltage-

15

tunable component could be used as a pre-filter to the ac-modulated MIRF in order to extend the temperature dynamic range without recourse to mechanically interposable attenuating filters.

4.3   Sensitivity to temperature changes

For a given level of uncertainty ΔS in the measured intensities, it can be shown using Eq. (11) that the error in the inferred visibility is given by

$$\Delta \zeta = \frac{2S_{\mathrm{max}}S_{\mathrm{min}}}{(S_{\mathrm{max}} + S_{\mathrm{min}})^2} \left(\frac{\Delta S_{\mathrm{max}}}{S_{\mathrm{max}}} - \frac{\Delta S_{\mathrm{min}}}{S_{\mathrm{min}}} \right) \tag{12}$$

Introducing the mean and difference signals $\bar{S} = (S_{\mathrm{max}} + S_{\mathrm{min}})/2$ and $S' = (S_{\mathrm{max}} - S_{\mathrm{min}})$, and approximating the combined fractional error [rightmost term in Eq. (12)] as $\Delta \bar{S}/\bar{S}$, we obtain

$$\begin{aligned} \Delta \zeta &= \frac{4\bar{S}^2 - S'^2}{16\bar{S}^2} \frac{\Delta \bar{S}}{\bar{S}} \\ &\approx \frac{\Delta S}{S} \end{aligned} \tag{13}$$

where in the last step we have ignored the difference term compared with $\bar{S}$ and for notational simplicity taken $\bar{S} = S$. If we approximate a linear relationship between visibility and the inferred temperature $\zeta \approx \alpha T$ (see Fig. 8), then, for a noise-limited radiometric temperature uncertainty ΔT_R, [see Eq. (4) and Eq. (8)] the resolvable change in temperature obtained by the probing the interferogram slope is

$$\Delta T = \frac{1}{\alpha} \frac{\Delta S}{S} \approx \frac{\rho(\bar{\lambda}; T)}{\alpha T} \Delta T_R \tag{14}$$

where $\bar{\lambda}$ is an intensity weighted mean wavelength in the spectral window of interest. As expected, this shows that the error in the tempeature estimate is roughly inversely proportional to the modulation depth. For a visibility $\zeta = \alpha T \sim 0.3$, the ability to resolve small temperature changes is worse by the factor $\sim 3\rho$ than methods based on absolute radiometry. The quantity $\rho(\lambda; T)$ varies slowly with wavelength and has a value of around 10 for temperatures of interest (see Fig. 2). The result is that for conditions under which $\Delta T_R \sim 0.1°$ we can expect the spectral estimate to be no more accurate than a few degrees. Similar degradations occur for any method relying on a spectral estimate alone (such as two-colour radiometry), but are more or less acceptable depending on the application.

4.4   Calibration and non-ideal effects

The MIRF spectrometer can be calibrated against a known greybody having its temperature independently determined using contact sensors. For monitoring

16

non-greybodies, a "slope" correction can be applied to compensate for the emissivity bias. Till now, we have not attempted to take account of atmospheric absorption effects, the spectral variation of transmission for component optics, depolarization and attenuation near 5μm due to the crystal absorption, or for the spectral dependence of the detector sensitivity. The sensitivity of MIRF to temperature changes arises because the two lowest order moments of the spectrum dominate the interferogram at small delay. If these two spectral averages are not severely affected, the temperature sensitivity of the system persists and can be quantified through appropriate calibration.

To illustrate this, we model the case where CO_2 and H_2O absorption completely eliminates the spectral emission in the range 4-4.3 μm and 2.7-3.3 μm. The applied spectral filter is overlaid on the blackbody spectra shown in Fig. 9 (a). The computed spectra are shown in Fig. 9 (b) and the time domain signals obtained for 2×10mm crystals with sinusoidal modulation of 3000V amplitude at an operating offset $L_0 = 50\mu$m are shown in (c). The dependence of the visibility on temperature is given in Fig. 9(d). Similar calculations which allow for the spectral dependence of the responsivity for cryogenically cooled InSb detectors are presented in Fig. 10. In both cases, despite strong distortion of the blackbody spectra, there is a clear link between the visibility and the source temperature.

Apart from atmospheric absorption effects, which may be difficult to quantify, fixed distortions such as detector responsivity and optical transmission can be accounted via a one-off system calibration against a greybody of known temperature.

5   Measuring temperatures greater than 1000K

Operation at higher temperatures is technically less challenging for a number of reasons:

1. the radiated power is larger,

2. λ_M is smaller so that drive voltages and crystal thicknesses can be reduced, or alternatively, a larger region of the interferogram can be probed.

3. optical materials and detectors are cheaper and more readily available. Detectors arrays such as near-IR CCD cameras do not require cooling.

The blackbody spectrum (not relatively normalized), interferogram and modulated signal obtained using the passband between 650nm and 1350nm for temperatures in the range 1000-3500K are shown in Fig. 11 for a crystal thickness 20mm, aperture 25mm, operating point (net delay) 40 μm and sinusoidal drive voltage of amplitude 3000V. Note that the modulation depth is significantly greater. This gives rise to a strong second harmonic component.
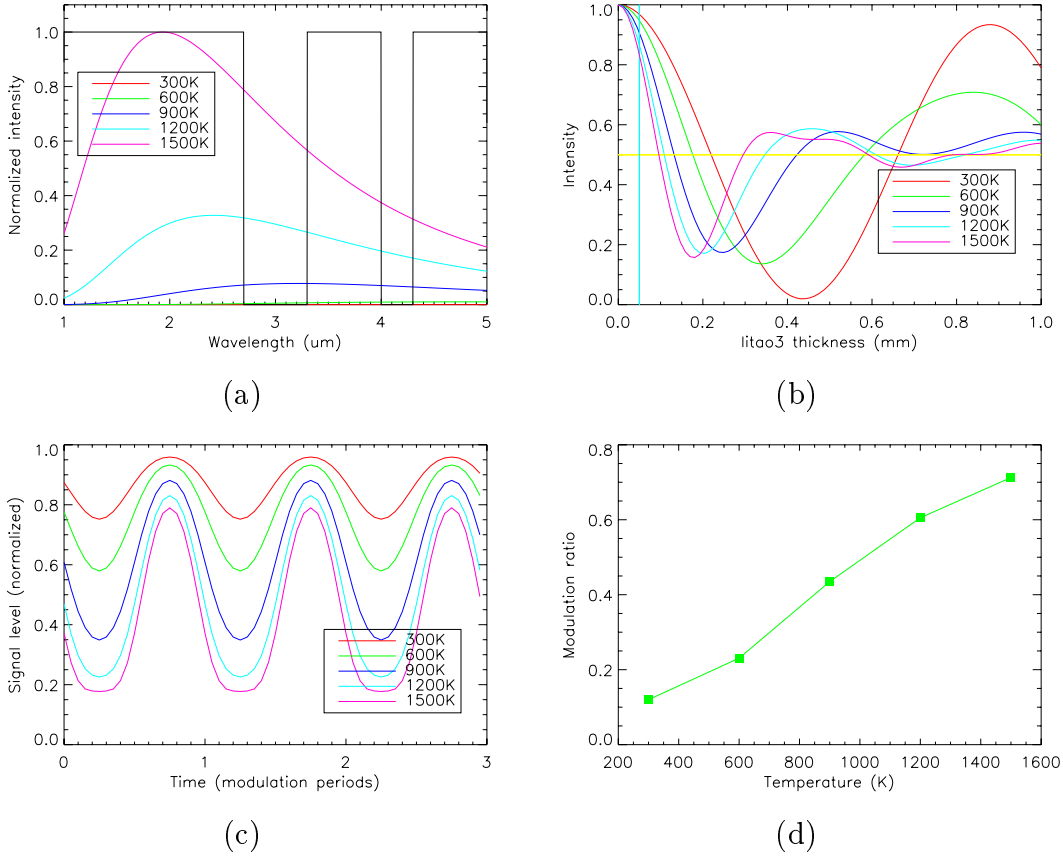
Figure 9: (a) Model atmospheric transmission factor overlaid on blackbody spectra for a range of temperatures; (b) the computed interferograms; (c) the calculated time domain signals and (d) the visibility as a function of source temperature.

5.1 Measurement strategy (b) - monitoring the turning points

Because of the greater modulation depths readily achievable in the vis-NIR region of the spectrum, a suitable strategy is to scan the interferogram about an operating point close to a peak or trough. The tangent of the second and first harmonic amplitudes measures the phase in the modulation cycle at which the interferogram turning point (related to λ_M) is encountered. An alternative is to take the ratio of the second harmonic and fundamental amplitudes as seen in Fig. 11(d).

As well as being sensitive to the source temperature, the sensitivity for a given temperature can be optimized by electrooptically tuning the operating point L_0 using a dc voltage bias. Conversely, one might also envision a system in which the dc bias is automatically tuned to maximize the harmonic ratio, thereby directly reading out the temperature. This is illustrated in Fig. 12 which shows
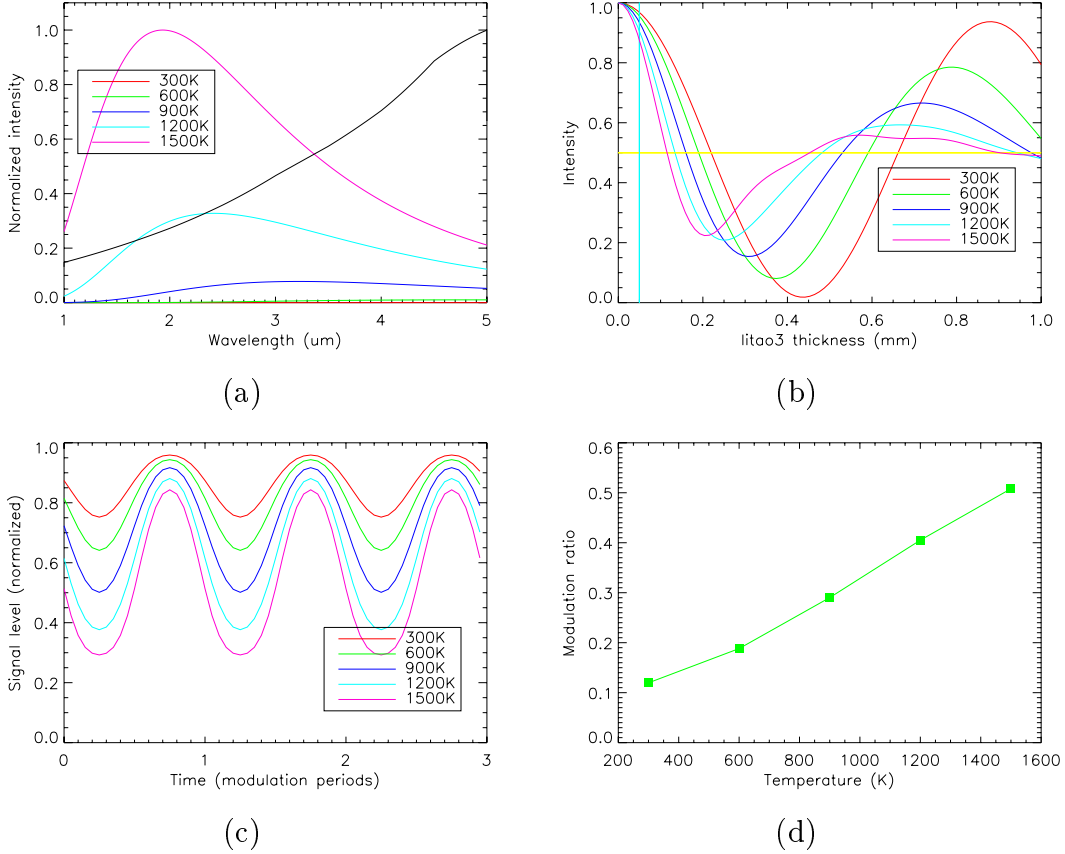
Figure 10: (a) Normalized spectral responsivity for InSb photovoltaic detectors overlaid on blackbody spectra for a range of temperatures; (b) the computed interferograms; (c) the calculated time domain signals and (d) the visibility as a function of source temperature.

the sensitive effect on the harmonic ratio of an imposed offset voltage of ± 10V. This opens the possibility for sensitive feedback control of a process temperature by tuning the operating point and maximizing the harmonic ratio. From the figure, it is clear that a SNR of around 200:1 is sufficient, in this case, to deliver temperature accuracy to 5°. The SNR can be improved by increasing the received optical bandwidth. This has the effect of separating the interferograms leading to harmonic ratios that vary more strongly with temperature change. The approach described here could be well suited to temprature monitoring/control in glass, ceramics and metals industries.

5.2 Measurement strategy (c) - monitoring the zero crossings

This is an essentially differential technique that relies on probing electrooptically either side of the zero crossing using dual birefringent electrooptic crystals. Moe
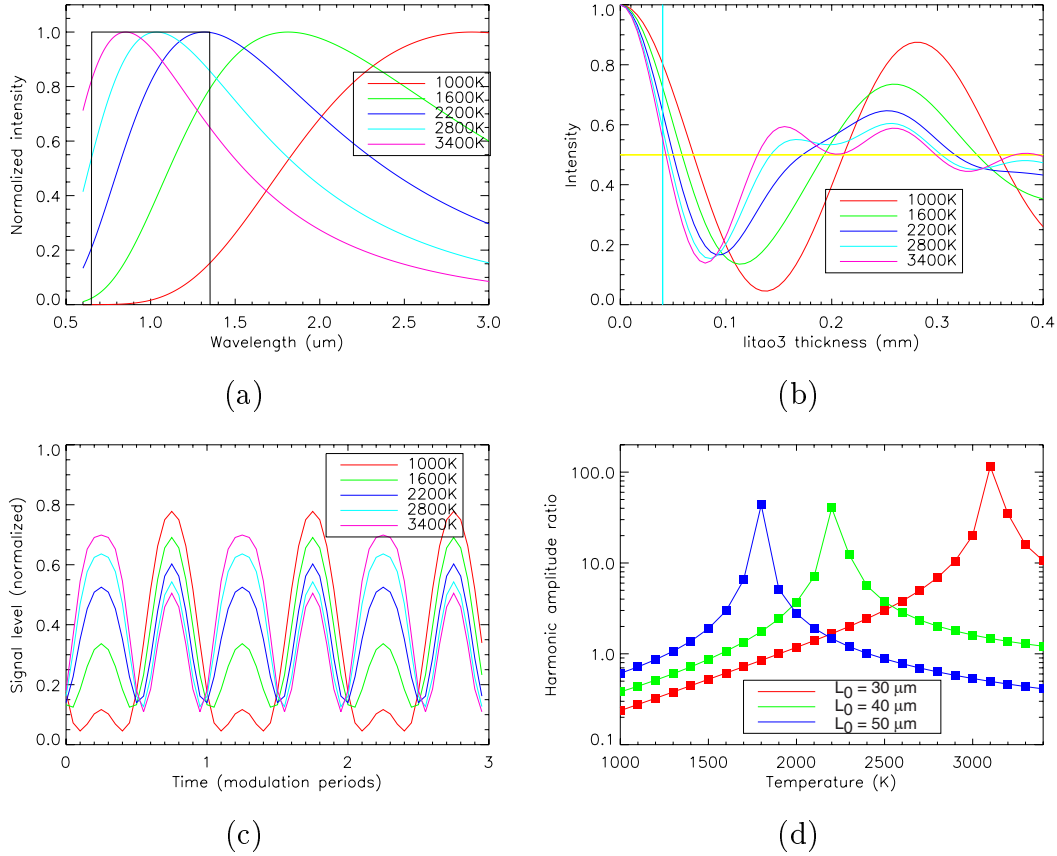
Figure 11: (a) Normalized blackbody spectra for high temperatures in the range 1000K to 3500K; (b) the corresponding interferograms; (c) the calculated time domain signals and (d) the harmonic amplitude ratio as a function of source temperature for operating points $L_0 = 30$, 40 and 50 μm.

to come ...

5.3 High temperature measurements in the mid-IR (2-5 μm)

When using the blue side of the Planck blackbody curve, it is clear that the power captured within a given passband will increase rapidly with temperature. This is both beacuse the radiant intensity is proportional to T^4 and because the spectrum peak shifts further into the measurement passband. As noted above, montioring systems which exhibit significant temperature variation, requires special measures to handle the wide intensity dynamic range.

An alternative strategy is to monitor the red wing of the spectrum. In this case, though the radiant intensity still increases dramatically with temperature, the spectral peak moves out of the passband. The received blackbody radiant
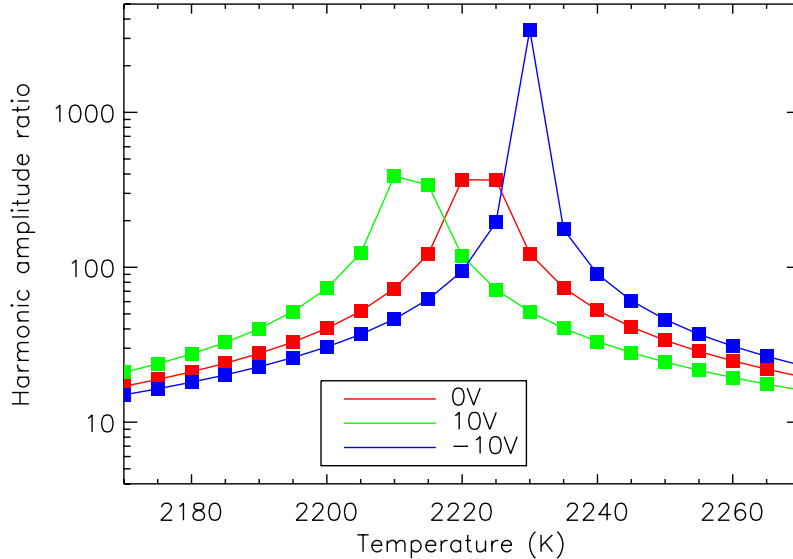
20

Figure 12: Variation of harmonic ratio as a function of temperature and for voltage tuning about the nominal operating point $L_0 = 40\mu$m.

power in the bands $2 - 5\,\mu$m and $0.6 - 1.2\,\mu$m as a function of temperature is shown in Fig. 13. The reduction in required intensity dynamic range is clearly evident. The effect is even more pronounced when the red-weighted sensitivity of the semiconductor detectors is included. Red wing measurements, while technically more demanding and expensive, offer some advantage for measurements requiring high dynamic range. However, sensitivity to temperature changes is poorer because the relatively slow spectral roll-off makes spectral disciminiation more difficult.

6 Experimental verification

We have set up an experiment using a filament lamp source and MIRF spectrometer based on two crossed LiNbO$_3$ crystals of length 50mm and aperture 25mm interposed between two broadband red-optimized (620-1000nm) polarizing beamsplitter cubes. Apertures of $\sim 3 - 5$ mm diameter were used to limit the light flux and to improve instrument fringe contrast. The latter is an issue only for the large thicknesses of LiNbO$_3$ used for these preliminary measurements (see Sec. 7.1). A Hamamatsu red-sensitive GaAs photomultipler tube (R943-02, 200-900nm) was used as detector. A PC-based DAQ card operating under "PC-MOSS"software control was used in conjunction with a high voltage amplifier to generate the modulating voltage (100Hz) applied to the crystals. The signals were synchronously acquired using the same PC-based DAQ system.
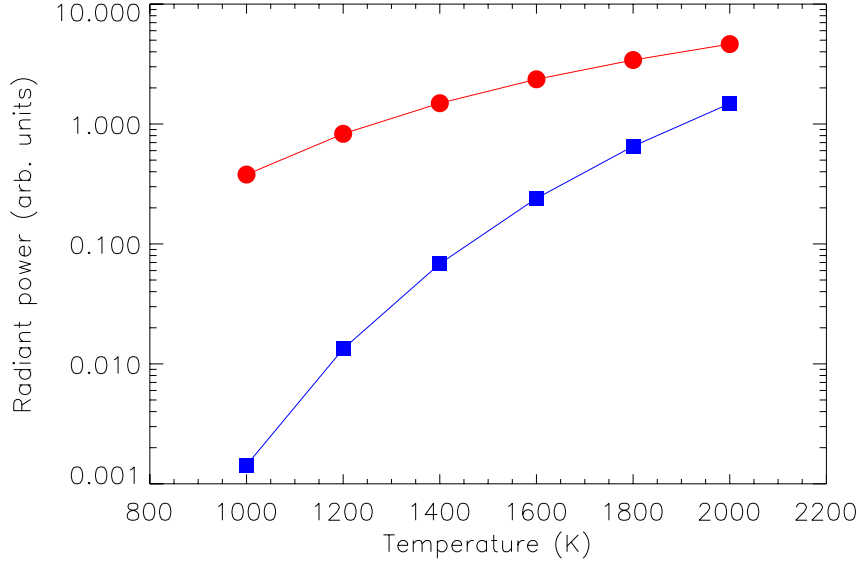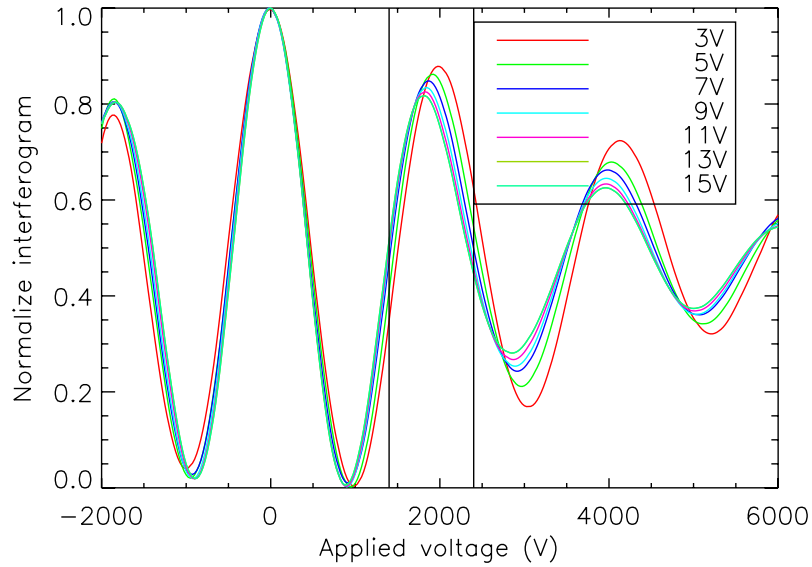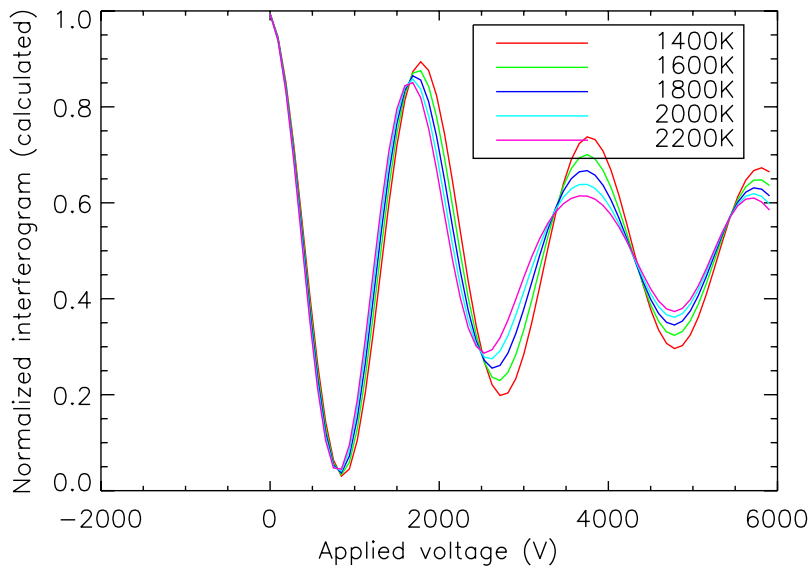
Figure 13: The variation of received power with temperature for red passband $2 - 5\,\mu m$ (circles) and blue $0.6 - 1.2\,\mu m$ (squares). There is a significant dynamic range advantage for red wing measurements.

Figure 14(a) shows a portion of the interferogram measured by applying a linear ramp of peak amplitude 4000V across the LiNbO$_3$ crystals. A bias offset of -2000V was required to compensate for a small mismatch in the crossed crystal lengths giving rise to incomplete dc cancellation of the optical path length. The bias allows a portion of the interferogram on both sides of the "white light" position (corresponding to zero net delay) to be measured. The interferograms have been arbitrarily normalized according to their minimum and maximum peak values. For comparison, Fig 14(b) shows calculated interferograms for a range of blackbody temperatures, assuming that only radiation in the band 600-900nm contributes to the interference signal. There is close similarity between measured and computed interferograms, including reasonable agreement about the electrooptic drive voltages required to probe the interferogram. The discrepancy may be due to the choice of effective optical bandwidth which has been used for the calculations.

The interferogram can be locally probed for sensitivity to temperature variations. This is done by applying a 200Hz sinusoidal modulation of amplitude 500V spanning the region indicated by the vertical lines in Fig. 14(a). The temperature (filament voltage) variation of the resulting time-domain signals is shown in Fig. 15(a). Using the PCMOSS system, we have slowly ($\sim$ 10s) swept the filament voltage while recording the interferogram. The calculated ratio of fundamental and second harmonic amplitudes is shown as a function of filament voltage in Fig. 14(b). The signals were averaged over 5 modulation periods ($\sim$ 25ms). The
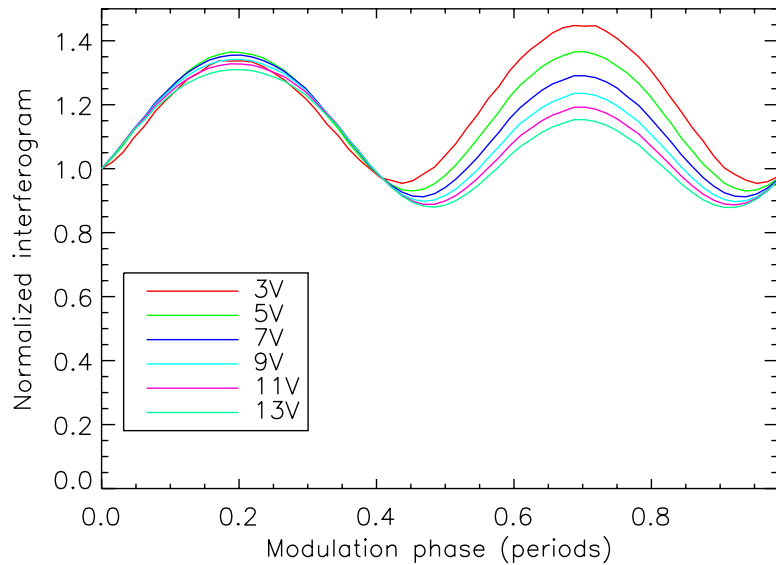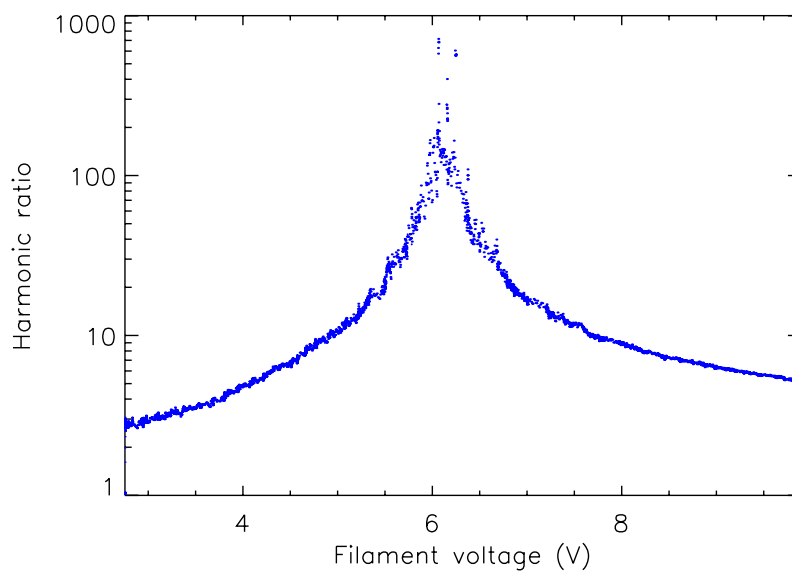
(a)

(b)

Figure 14: (a) Measured interferogram as a function of filament voltage and (b) computed interferograms for temperatures in the range 1400K to 2200K. See text for discussion.

sensitive dependence on filament voltage (temperature) is evident. The current in the filament was increased slowly by hand over a period of around 5-8 s. Small irregularities in the resulting ratio curve are due to variations in the rate of increase of the the filament current and the thermal time constant of the filament. The signal to noise ratio increases at larger voltages due to the increased brightness of the lamp.

The trace width indicates that the filament voltage can be determined within ± 0.04V corresponding roughly to a resolvable temperature change of a few degrees Kelvin. Better resolution could be obtained by increasing either the integration time or the spectral bandwidth.

(a)

(b)

Figure 15: (a) Measured time-domain modulation signal as a function of filament voltage and (b) corresponding harmonic ratios.

7 MIRF infrared imaging thermography

Being a simple transmissive eo-modulated device, MIRF can be mounted as a prefilter to a standard infrared imaging camera. As an absolute temperature deivce, it allows the emissivity of objects in the field-of-view to be determined, in turn allowing the IR camera to be absolutely calibrated. Alternatively, in applications requiring accuracy rather than high precision, MIRF can remain fixed in place.

A simple strategy for processing the modulated signals is to lock the modulation frequency to half the camera frame rate. In this case, the gated and integrated detector charge in sequential frames can be synchronized to coincide with the peak and trough of the interferogram. The sum and difference of successive frames can be computed by a DSP and the image ratio compared with a calibration look-up table in order to form the absolute temperature image. An alternative is to choose a modulation frequency that is somewhat higher than the frame rate, but which is appropriately subsampled by the detector array. Duty cycle issues must be addressed (i.e. ratio of signal capture time to inter-frame period).

MIRF can be fabricated as a compact sealed unit that can be mounted to the front of an infrared imaging camera. The electronic hardware for processing and comparing sequential frames can stand independently of the camera, provided the camera makes the image digitally available.
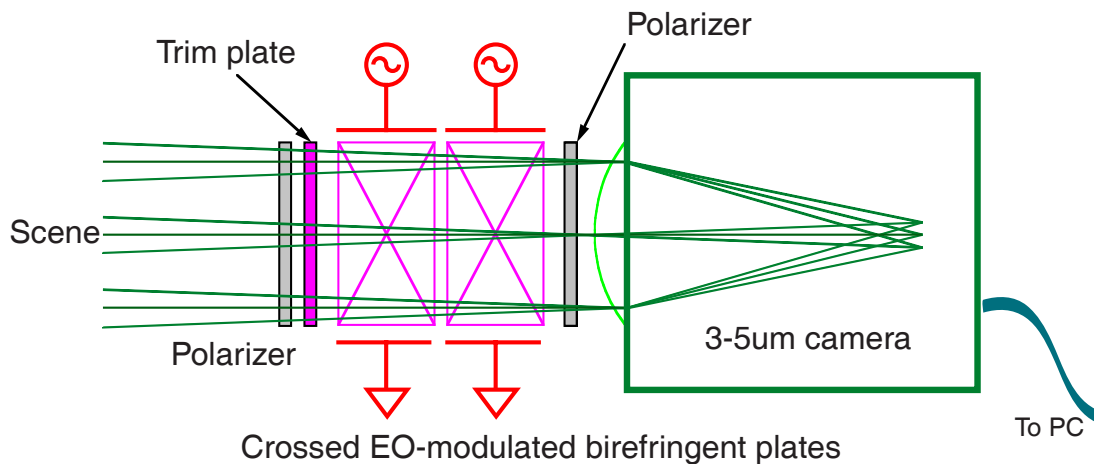

Figure 16: Scematic of optical layout for the imaging MIRF combined with commercial mid-IR digital camera.

At higher temperatures it may be possible to use visible optics and CCD arrays in the range 650nm - 1050nm, thereby considerably reducing cost. The harmonic ratio method would work well in this range. Large aperture (50 mm)

wide field-of-view (20 °) imaging cameras operating at modest drive voltages (4 kV amplitude) and plate thicknesses of 20 mm would result in harmonic ratio sensitivities as shown in Fig. 17. To measure the harmonic ratios, it would be necessary to sample the interferometric image at four points in the modulation cycle. A simple algebraic manipulation of these frames using DSP hardware would yield the harmonic ratio image and hence the temperature distribution. The effective time resolution would be a quarter of the maximum CCD frame rate.
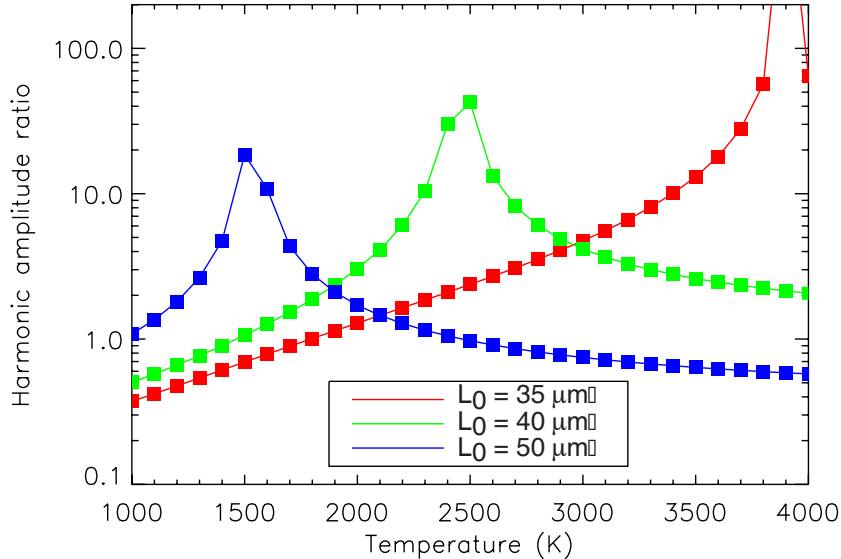

Figure 17: Variation of harmonic ratio as a function of temperature for operating points $L_0 = 35$, 40 and 50 μm. Blackbody radiation in the visible/NIR band 650nm to 1050nm has been used in this calcualtion.

7.1 Field-of-view

The average over the range of angles subtended by the source gives rise to an instrument contrast degradation that reduces the apparent visibility. For a free-space Michelson interferometer, the range of collected ray angles gives rise to a pattern of concentric rings in the interferometer image plane. Uniaxial birefringent plates (such as $LiTaO_3$ or $LiNbO_3$) give rise to a saddle-like hyperbolic fringe pattern as shown in Fig. 18 for parameters $L = 10$ mm and $\lambda_0 = 3.5\,\mu$m.

By the van Cittert-Zernike theorem, the mutual coherence of the interfering waves at the detector on axis is obtained by integrating over the source irradiance distribution. For a uniform, monochromatic circular source of solid angle $\Omega =$
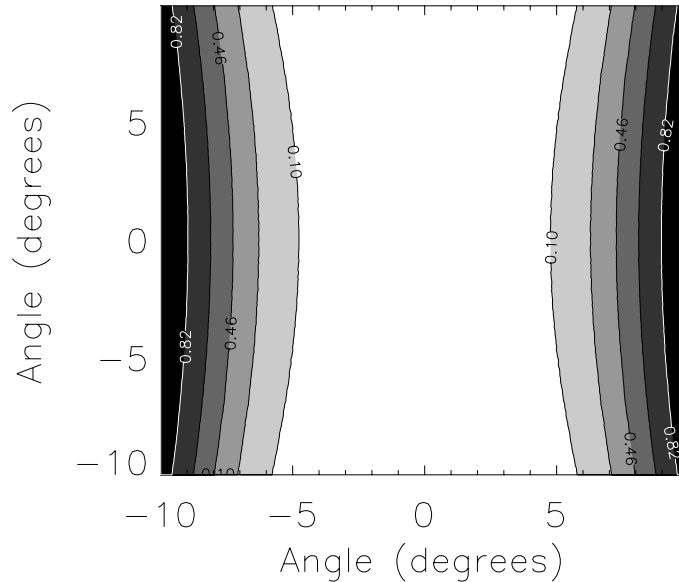
Figure 18: The angular dependence of the hyperbolic fringe pattern produced by a LiTaO$_3$ birefringent plate of thickness 10mm at wavelength 3.5 μm

$\pi\theta_{\max}^2$, the instrument contrast is given approximately by [6]

$$\zeta_I = 1 - \frac{\Omega^2 N^2}{12n^4} \qquad (15)$$

where N is the crystal birefringent delay in waves. Given $L = 10$ mm and $\lambda_0 = 3.5\,\mu$m, the optical delay for weakly birefringent LiTaO$_3$ is $N \approx 13$ waves. In this case, the field-of-view giving rise to 10% degradation in instrument contrast is $2\theta_{\max} \approx 22°$. By contrast, for LiNbO$_3$ we have $N = 176$ and $2\theta_{\max} \approx 2°$.

For interference spectroscopy with quasi-monochromatic sources, field-widening techniques involving the use of crossed birefringent plates with an interposed half wave plate at 45° azimuth can significantly improve the available field-of-view. The small coherence length of the IR emission, however, gives rise to a super-position of interferograms at a multiplicity of delays leading to complications in interpretation. We must then be content with the quite adequate natural field-of-view available using LiTaO$_3$ crystals of modest thickness.

For an imaging MIRF system, we must integrate over the range of wavelengths traversing the filter and account for off-axis angular effects when estimating the instrument contrast. In practice, these effects, as well as other instrumental effects relating to spectral weighting as noted above, must be accounted through a one-off calibration of the entire imaging system using a greybody of known temperature.

When field-of-view issues are critical, an attractive alternative approach is to use a Z-cut modulating cell and a fixed Y-cut "trim plate" to obtain the optical

delay. Because the Z-cut plate is not naturally birefringent, the field-of-view is limited only by the thickness of the trim plate which has a net delay $N \lesssim 1$. The trade-off is that a higher drive voltage may be required to obtain the required modulation depth.

8 Outlook for the future

8.1 Current status

The ideas presented here are based on simulation results. There is reason to be confident, however, given the success of the MOSS camera and its variants, which are founded on a similar concept. The requisite technologies, namely filters, polarizers, detectors and detector arrays are well developed. Indeed, the constraints on crystal quality are substantially less severe for the IR application. Figure 19 is a photograph showing the MOSS camera and calibration optics installed on the H-1 heliac, a high temperature toroidal plasma magnetic-confinement device in the Plasma Research Laboratory.
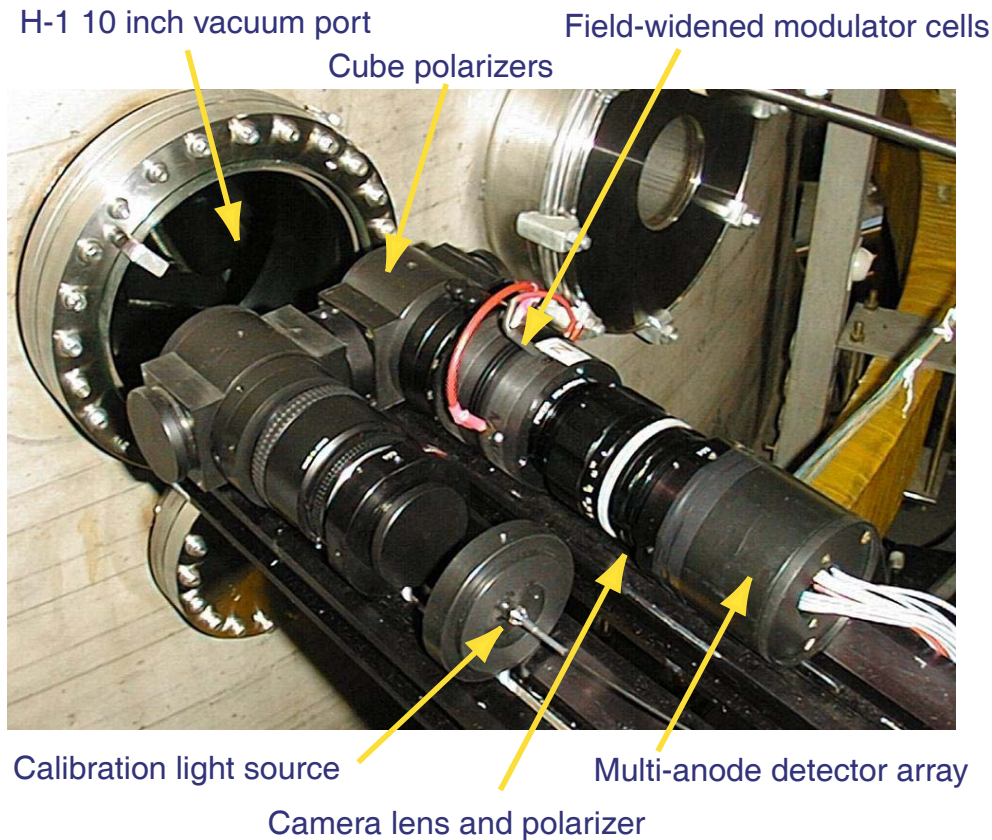

Figure 19: The MOSS camera and calibration optics imaging the plasma ion temperature and flow speeds in the H-1 heliac.

8.2 Advantages and benefits

MIRF shares the abovenoted advantages of other spectrally discriminating techniques such as two colour pyrometry. In this area, there is presently extensive research into the development of dual band infrared focal plane arrays (FPA) primarily for military applications. The idea is to use interlaced [7] or overlaid arrays [8] sensitive in separate spectral regions and to use the image ratio to infer the source temperature. These devices are difficult and expensive to fabricate and require cryogenic cooling.

Using MIRF, the spectral information is multiplexed temporally (via the modulation cycle) rather than onto two separate detector arrays or through separate rotating filter elements. The alternative techniques are either expensive or cumbersome or both. For imaging applications, MIRF offers spectral sensitivity using a only single array of cryogenically cooled InSb (for mid IR) or recently developed room temperature microbolometer FPAs. An overview of the current state-of-the-art in commercial IR detector technology can be found at `http://www.everettinfrared.com/detectors.htm`.

Time-domain multiplexing has the additional important advantage of allowing the system to be integrated with room-temperature pyroelectric detector arrays which respond only to ac signals. Moreover, 1/f fixed pattern noise is eliminated when the modulation frequency is greater than the 1/f noise knee (usually around 10Hz or less). For single channel systems, important SNR advantages accrue with the ability to use sensitive phase-locked detection of the modulated IR signal.

For higher temperature applications, we have demonstrated that simple visible to near-IR technologies are capable of providing accurate temperature measurements. This is an important practical advantage over standard two colour IR instruments.

8.3 Potential applications

There are hundreds of websites referring to applications of IR thermometry, including discussions of the pros and cons of simple radiometric and two-colour approaches. There appear to be no references to fixed birefringent plate systems such as MIRF. `http://www.nedians.8m.com/pyro.html` is a useful source of information regarding the state-of-the-art in remote temperature sensing and sensing applications.

8.3.1 IR camera calibration

Attached as a prefilter to a single channel or imaging infrared radiometer, MIRF allows the source emissivity to be immediately determined. MIRF can then be removed and this information used subsequently for sensitive absolute temperature montioring.

8.3.2 Process control

Industrial process applications of radiation thermometry include the heat treating, forming/extrusion, tempering, and annealing of glass, metals plastics and rubber, quality control in the food and pulp and paper industry, and curing processes for resins, adhesives, and paints. Non-contact temperature sensors have been used and will continue to be valuable for research in military, medical, industrial, meteorological, ecological, forestry, agriculture, and chemical applications. Regular absolute temperature calibration is a must in these applications. This can be provided simply and routinely by MIRF without the need for an expensive blackbody source.

8.3.3 Military surveilance

As well as military applications which require absolute temperature information, MIRF can reconfigured to allow IR emissivity-based discrimination of missile/aircraft engine spectral signatures. This is the subject of a research and development proposal with DSTO.

8.3.4 Plasma physics

The first wall and plasma limiter tiles in a fusion tokamak are subject to heat loads up to 5MW/m^2. It is known that the emissivity can vary substantially with temperature for most metals and certain other materials. It is therefore vital that robust spectrally-based thermographic tools be used to monitor the heat flux to plasma facing components. MIRF is ideally suited to this application.

8.3.5 Medical diagnostics

Infrared imaging devices also are used for thermography, or thermal imaging. In the practice of medicine, for example, thermography has been used for the early detection of breast cancer `http://www.villemariemed.com/functionalinfrared.htm` and for the location of the cause of circulatory deficiencies leading to local heating and inflammation which can be located with an infrared imager. MIRF would allow routine absolute calibration of existing high-resolution radiometric imagers.

8.4 Development plan

Given a satisfactory appraisal of market potential, the following is how the R&D could proceed. It is not clear at this stage if the more technically challenging aspects should be developed in the School, by an outside company or as a spin-off enterprise.

1. Build/test/verify a prototype single channel system. This is sufficiently close to the proposed DSTO work that development could proceed in parallel with, and sharing optics/hardware purchased out of the DSTO grant.

2. Modify pre-existing PC-card/LabVIEW software package for signal acquisition/process/display. This will also be part of the DSTO contract.

3. Explore operation in visible near-infrared for medium-high temperature sensing. Develop phase sensitive measurement system based on harmonic ratio estimate.

4. Develop standalone hardware system for single channel MIRF spectrometer with digital readout. This would include collection optics/fibre system, modulator and associated electronics, detector module, data acquisition/processing, control/display. This and following phases would require capital funding.

5. Develop/test add-on calibration MIRF for IR camera. This would include a sealed electrooptical package with standard optical fittings, integrated controller, modulator, digital frame grabber, DSP and false colour display. This would be suitable as a retrofit to an exisiting mid-IR camera, possibly to be used for absolute calibration purposes or as an accessory for routine absolute thermography.

6. Develop/test integrated MIRF-based absolute thermographic camera.

If successful, it would be worth exploring extending the approach into the near IR and visible for sensing of higher temperatures. Technologies become much simpler in this region.

References

[1] P. C. Dufour, N. L. Rowell, and A. G. Steele, Appl. Opt. **37**, 5923 (1998).

[2] J. Howard, Appl. Opt. (Accepted for publication) (2001).

[3] J. Howard, C. Michael, F. Glass, and A. Cheetham, Rev. Sci. Instrum. **72**, 888 (2001).

[4] S. A. Kazi and H. I, J. Appl. Phys. **80**, 6561 (1996).

[5] C. C. DAVIS, *Lasers and Electro-Optics* (Cambridge University Press, Cambridge, 1996).

[6] W. Steel, *Interferometry* (Cambridge University Press, Cambridge, 1967).

[7] S. Gunapala *et al.*, Infrared Phys. and Tech. **42**, 267 (2001).

[8] L. H.C. *et al.*, Infrared Phys. and Tech. **42**, 163 (2001).